INTERNATIONAL JOURNAL FOR NUMERICAL METHODS IN FLUIDS, VOL. 10, 411–428 (1990)

A PROPER ORTHOGONAL DECOMPOSITION OF A SIMULATED SUPERSONIC SHEAR LAYER

M. KIRBY, J. P. BORIS* AND L. SIROVICH

Center for Fluid Mechanics, Turbulence and Computation, Division of Applied Mathematics, Brown University, Providence, RI 02912, U.S.A.

SUMMARY

The Karhunen–Loève procedure is applied to the analysis of an ensemble of snapshots obtained from a conditionally sampled localized shear layer simulation. The computed set of *optimal* basis functions is used to economically characterize sampled flow realizations. Pictorially it is seen that the essential features (and roughly 80% of the energy) of typical flows are captured by retaining roughly 10–20 parameters in the expansion. Smaller-scale features are resolved by retaining more terms in the series.

KEY WORDS Proper orthogonal decomposition Karhunen–Loève expansion Data compression Large-scale structure Supersonic shear flow Flux-corrected transport

1. INTRODUCTION

The existence of coherent motions in fluid flows rich in complex behaviour is by now well established. For a comprehensive review article on organized motion in turbulence, see Cantwell.[1] In principal, an ability to extract the structure of a flow and incorporate it into its description should reduce the parametrization, or the amount of information, needed to quantify the flow. In this study we apply a statistical procedure, which has been widely used in the study of turbulent flows, for the extraction of structure in a supersonic shear layer. As outlined below, the approach provides a concrete mathematical framework in which to discuss the high-energy components of the flow and may potentially lead to a reduced dynamical model.

The analytical methods are based on Lumley's proper orthogonal decomposition[2–4] (referred to in pattern theory as the Karhunen–Loève (K–L) expansion and in the statistical literature as principal component analysis). The procedure is useful for systematically and efficiently characterizing an ensemble of inhomogeneous patterns which possess a high degree of organized structure. Lumley proposed the proper orthogonal decomposition as an objective method for determining coherent structures. However, the connection between the eigenfunctions derived by the decomposition and the coherent structures observed in simulations and experiments is still unclear. For a more detailed discussion of these and other points see References 5 and 6.

The method provides a low-dimensional representation of a characteristic large-scale structure by decomposing it into a set of uncorrelated, data-dependent components. The components are the eigenfunctions of a two-point correlation tensor and the expansion is *optimal* in several senses. For instance, the K–L eigenfunctions minimize the mean square error and maximize the total

* Permanent address: Naval Research Laboratory, Washington, DC 20375, U.S.A.

0271–2091/90/040411–18$09.00

Received 1 December 1988
Revised 23 June 1989

energy captured in each co-ordinate direction, subject to orthogonality constraints. Also, while the method is optimal with respect to second-order moments, there is no loss of higher-order moment information since the eigenfunctions form a complete basis. However, the efficiency with which higher-order information is captured is not prescribed by any optimality condition. There exist many references for the details of the properties of the K–L expansion, e.g. References 7–13.

The object of this paper is not to enter into the somewhat controversial deliberations as to definitions and methods for the eduction of coherent structures.[14,15] With this in mind we will take the following utilitarian view: structures which satisfy a well-defined sampling condition will be treated as the objectively selected large-scale phenomenon of interest. This approach has been applied in two other investigations, similar in spirit, to extract large-scale structures in an experimental and numerical jet flow.[16,17] For the flow under consideration, a large-eddy simulation of a localized supersonic shear layer, the structures of interest are clearly identifiable; they consist of two dynamic shocks whose position and strength vary in time, bounding a central high-pressure region. A detailed description of the flow for a range of Mach numbers is available in Reference 18. The sampling condition used to generate an ensemble of flow realizations is described in Section 3.

It is well known that the methods suggested here require a great deal of data to provide sufficient statistics for the computation of the eigenfunctions. This problem can be mitigated in part by exploiting the symmetry group of the flow and consequently extending the data. For the current problem this extension cuts the expense of the computations in half. In addition, the extension imposes evenness and oddness on the eigenfunctions of the two-point correlation tensor, a fact which provides further characterization of the flow.

This framework allows the characterization and data-compressed representation of a flow in terms of a fixed set of symmetric *eigenflows*. While these eigenflows are not in general solutions of the flow equations, they can clearly be viewed as corresponding to mechanical motions and as such provide insight into the relative make up of each flow realization in terms of its *eigenstructure*. When the flow is decomposed in this manner, pictorially we see that its large-scale features are captured using a small number of eigenfunctions.

2. NUMERICAL SIMULATION

2.1. Flow description

Two parallel supersonic streams of equal and opposite velocity are separated by a thin plate with a slot in the centre. The velocity of the opposing flows is 530 m s^{-1}, corresponding to a free stream Mach number of 1·6. Two sample flow realizations are shown in Figure 1. The gap, which horizontally spans 50% of the flow, creates a region of interaction between the two opposing streams. As the flow bends around the plate it collides with the oncoming stream, forming a shock. The 180° rotational symmetry of the geometry and boundary conditions results in roughly symmetrical features to the flow. The pair of shocks bound a central region of high pressure which contains a time-varying quantity of circulation. Also, there is a region of rarefaction and vorticity between each plate and the deflected stream. The long-term dynamics of the flow consists of *breathing*, i.e. variation in the distance between the two shocks (in the plane of the slot), and *sloshing*, i.e. overall lateral movement of the centre of the coherent structure. In addition there is the gradual accumulation and shedding of vorticity from the shear layer.

Preliminary investigations of a 3D simulation for this flow, at the same resolution, indicate that it is dominated by 2D effects, with 3D disturbances decaying in time. However, at this stage it is unclear what effect increasing the resolution will have on the simulation.

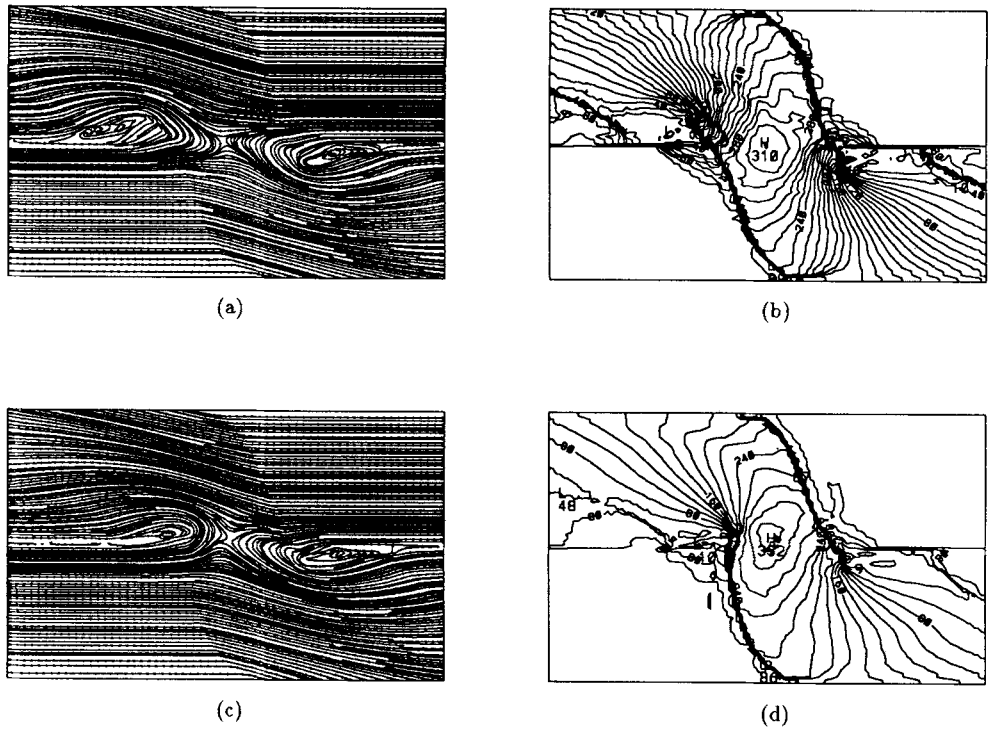

Figure 1. (a) Instantaneous streamlines of a typical flow realization. (b) Pressure field for realization (a). (c) Instantaneous streamlines of a second flow realization. (d) Pressure field for realization (c)

2.2. *Numerical model*

The numerical simulation, detailed in Reference 19, solves the time-dependent compressible conservation equations for a polytropic gas:

$$\frac{\partial \rho}{\partial t} + \frac{\partial}{\partial x_j}(\rho u_j) = 0, \tag{1a}$$

$$\frac{\partial}{\partial t}(\rho u_i) + \frac{\partial}{\partial x_j}(\rho u_i u_j) + \frac{\partial P}{\partial x_i} = 0, \tag{1b}$$

$$\frac{\partial E}{\partial t} + \frac{\partial}{\partial x_j}[(E+P)u_j] = 0. \tag{1c}$$

The equation of state is

$$E = \frac{P}{\gamma - 1} + \tfrac{1}{2}\rho u_i^2,$$

where E, P, γ, ρ and $\mathbf{u}$ denote the internal energy, pressure, ratio of specific heats, density and velocity respectively. The flow is assumed to be inviscid and non-heat-conducting.

Two-dimensional solutions are constructed using direction splitting and time step splitting with a one-dimensional, fourth-order, phase-accurate flux-corrected transport (FCT) algorithm. FCT is an efficient, non-linear monotone method which incorporates, at least qualitatively, most

of the local and global effects of the unresolved turbulence expected of a large-eddy simulation.[18] The computations are carried out at standard temperature and pressure on a 120 by 80 grid; thus a typical realization consists of $O(10^4)$ points. The upper and lower boundaries are free, while the inflow and outflow velocities are fixed on the appropriate vertical boundaries. The outflow boundary conditions are continuity conditions developed for such flows.[20]

3. PRELIMINARIES: SAMPLING, SYMMETRY AND FLUCTUATIONS

We apply the analysis to three two-dimensional flow variables generated by the numerical simulation, i.e. the pressure p and the horizontal and vertical momentum densities ρu and ρv. For convenience we will consider the flow variables to be scalar functions of $\mathbf{x}=(x, y)$. We omit the density from our analysis since in this problem it behaves in a manner analogous to the pressure field.

In order to obtain independent events we select only realizations, or *snapshots*, that satisfy a predetermined strobe condition. We choose as this strobe criterion the condition that the distance of either shock from the centre of the slot, in the plane of the plate, is a passing maximum. This allows us to include only large-scale structures which are approximately in the same stage of development, roughly eliminating time dependence from the problem. One could also view this procedure as a reduction of the space of admissible solutions. In doing this we do not reduce the generality of the approach, since intermediate strobe conditions can be sampled and the individual analyses then viewed as a whole. Indeed, this approach is necessary to derive evolution properties of the system and its decimated expansion.

As mentioned earlier, flow symmetry can be exploited to reduce the computational expense of the simulation. It is a simple task to verify that if

$$(\rho u(x, y), \rho v(x, y), p(x, y))$$

is a solution of (1), then so is

$$(-\rho u(-x, -y), -\rho v(-x, -y), p(-x, -y)).$$

This procedure results in extension of the data, since every *computed* flow produces two flows for use in the ensemble. In addition it can be shown that this type of extension imposes even and odd symmetry on the eigenfunctions.[21,22]

The ensemble average of a collection of snapshots is defined as

$$\bar{p}(\mathbf{x}) = \frac{1}{M} \sum_{n=1}^{M} p^{(n)}(\mathbf{x}) = \langle p^{(n)}(\mathbf{x}) \rangle, \tag{2}$$

where M is the number of snapshots in the ensemble. The extended ensemble average for the pressure field is then

$$\bar{p}(x, y) = \frac{1}{2M} \sum_{n=1}^{M} (p^{(n)}(x, y) + p^{(n)}(-x, -y)). \tag{3}$$

Throughout the rest of this paper we focus on the fluctuating quantities of the flow variables; e.g. the fluctuating pressure field is given by

$$p'(\mathbf{x}) = p(\mathbf{x}) - \bar{p}(\mathbf{x}). \tag{4}$$

However, for convenience we drop the primed notation.

4. KARHUNEN–LOÈVE EXPANSION

4.1. Formulation

The Karhunen–Loève expansion is based on representing a typical realization of a flow in terms of the eigenfunctions of the integral equation

$$K_{ij}(\mathbf{x}, \mathbf{x}')u_j^{(n)}(\mathbf{x}') = \lambda^{(n)}u_i(\mathbf{x}), \tag{5}$$

where summation and integration conventions are assumed. The two-point correlation tensor is defined by

$$K_{ij}(\mathbf{x}, \mathbf{x}') = \langle \phi_i(\mathbf{x})\phi_j(\mathbf{x}') \rangle, \tag{6}$$

where we have formed the concatenated variable

$$\boldsymbol{\phi} = (\rho u, \rho v, p). \tag{7}$$

The kernel K given in (6) is symmetric and non-negative; thus we have orthogonal eigenfunctions and non-negative eigenvalues. The kernel is also degenerate, a fact which greatly simplifies the actual computation of (5). In fact, using symmetry considerations one can show that the dimension of the discrete eigenvector calculation is always M (not $2M$), the size of the unextended ensemble. In addition, the cost of the calculation increases only linearly with the number of flow variables concatenated in (7).

Once we have computed the eigenfunctions, we can approximately *reconstruct* any member of the ensemble by an N-term expansion with

$$\boldsymbol{\phi}^N = \sum_{k=1}^{N} a^{(k)}\mathbf{u}^{(k)}, \tag{8}$$

where

$$a_k = (\boldsymbol{\phi}, \mathbf{u}^{(k)}) \tag{9}$$

under the normal Euclidean inner product. When $N = 2M$ this reconstruction is exact, since in this case the expansion is equivalent to a linear change of basis. The error introduced when the series is truncated represents the *true* error only if the ensemble spans the set of all admissible solutions. Since we do not know in advance just when the ensemble will be large enough, this error estimate is in fact only a lower bound for the error, on average. However, an upper bound on the error can be obtained by considering the *approximation* of snapshots which satisfy the strobe condition but were not included in the ensemble used to compute the eigenfunctions. The difference between these two error estimates should diminish, and eventually go to zero, as the number of flows in the ensemble becomes large enough.[22] Thus, to test the success of the method we will examine the efficiency of the expansion for both reconstructions and approximations of typical flows.

We use the Euclidean distance between the exact flow field $\boldsymbol{\phi}$ and its N-term expansion $\boldsymbol{\phi}^N$,

$$E_N = \frac{\|\boldsymbol{\phi}^N - \boldsymbol{\phi}\|}{\|\boldsymbol{\phi}\|}, \tag{10}$$

as a quantitative measure of the error of the approximation. In equation (10) $\boldsymbol{\phi}$ is understood to be the mean added flow, i.e. not the fluctuating field.

4.2. *Scaling*

The eigenfunctions of (5) are sensitive to the scaling of the flow variables ρu, ρv and p. This is especially of concern since the flow variables are in different units and have widely varying magnitudes. With this in mind we determine three scale factors which force the magnitude of the fluctuating variables to be, on average, $O(1)$. For example we compute the pressure scale factor by

$$s_p = 1 \Big/ \left\langle \sqrt{\left(\frac{1}{N_h N_v} \sum_{ij}^{N_h N_v} p_{ij}^{(k)} \right)} \right\rangle, \tag{11}$$

where $N_h = 120$ and $N_v = 80$ represent the horizontal and vertical dimensions of the grid.

5. RESULTS

5.1. *Ensemble averages and fluctuating quantities*

The ensemble averages of the components of ϕ are computed over 130 realizations, including the extended data, and are shown in Figure 2. We see that the ensemble-averaged streamlines and pressure field have several interesting features. The instantaneous streamlines of the ensemble-averaged velocity fields are shown in Figure 2(a). We observe that there is a critical distance from the plate, on the vertical boundaries of the flow, above which a particle entering is unlikely to pass through the slot, the below which is generally does. We refer to this streamline originating at the critical distance as a *separatrix*. The ensemble-averaged pressure field is shown in Figure 2(b). As one would expect, the centre of interaction is a high-pressure region. The shocks have been smeared somewhat, though we still see a steep pressure gradient on the symmetrical edges of the average-sampled structure.

The fluctuating components of the momentum densities and pressure field for the two sample flows shown in Figure 1 are computed according to equation (4) and shown in Figure 3. The figures are enlarged to show only the region of interaction, i.e. the middle 50% of the simulation, bounded on the left and right by the plates. Observe that the flows are very dissimilar and will provide a good comparison of the approximations carried out in Section 5.4. For instance, the

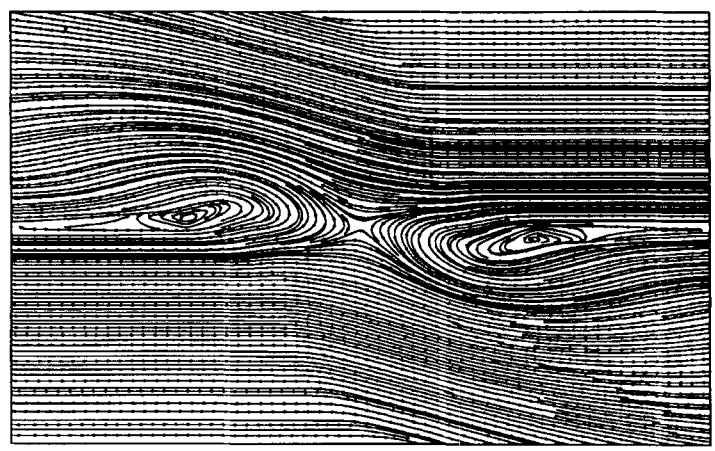

(a)

Figure 2(a)

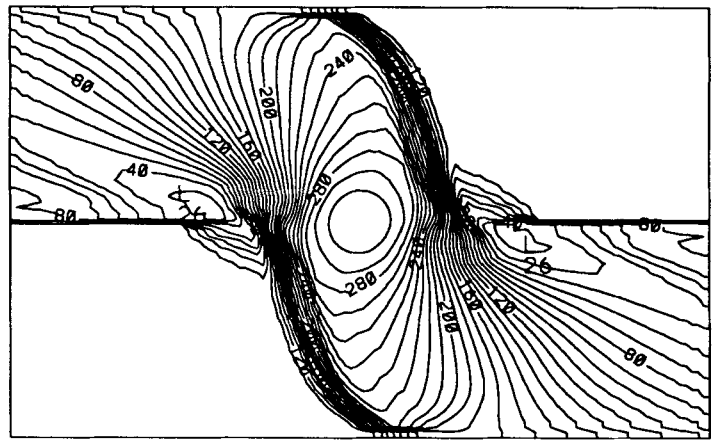

(b)

Figure 2. (a) Instantaneous streamlines of ensemble-averaged velocity fields. (b) Ensemble-averaged pressure field. The extended ensemble size is 130

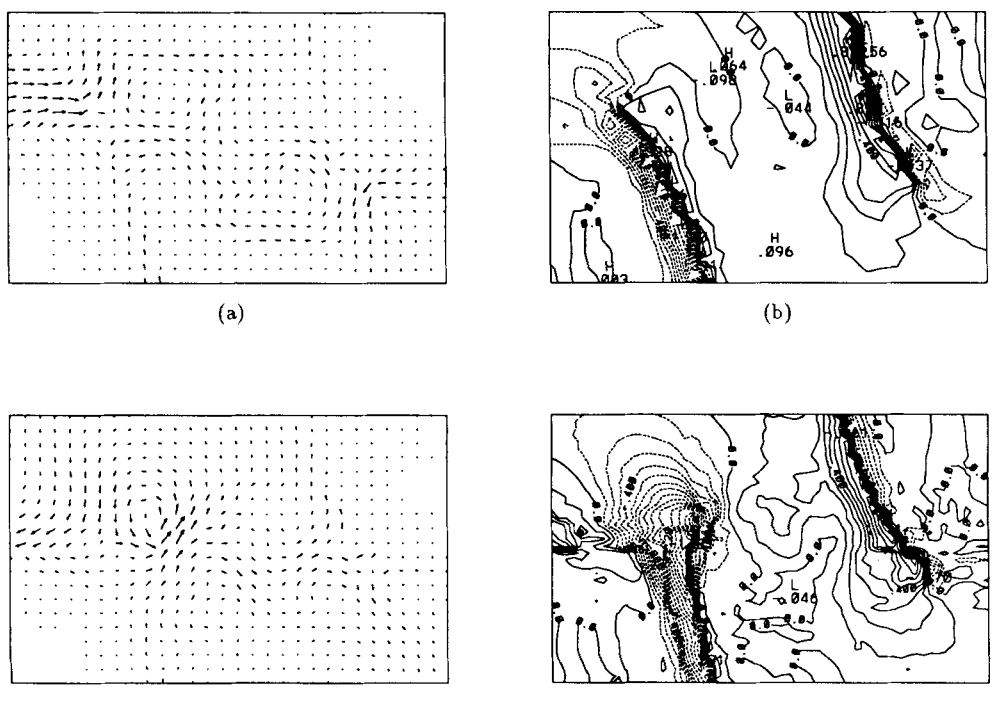

(a) (b)

(c) (d)

Figure 3. (a) Fluctuating momentum density field for Figure 1(a). (b) Fluctuating pressure field for Figure 1(b). (c) Fluctuating momentum density field for Figure 1(c). (d) Fluctuating pressure field for Figure 1(d). All the above plots, and those which follow, are blown up to show only the area between the plates

momentum density fields are composed of a complicated arrays of vortex-like structures, differing both in strength and location. Also we see that the fluctuating pressure fields have one common pronounced feature, i.e. shocks. This reflects the fact that the ensemble-averaged pressure field is smoother than an individual realization. Hence subtracting the mean field will not remove the shock structure. In addition, there are lobes of high pressure located roughly symmetrically at the end of each shock.

5.2. *Eigenvalues*

The eigenvalues (normalized by $\sum_{i=1}^{2M} \lambda^{(i)}$) resulting from equation (5) are shown in Figure 4. A Karhunen–Loève global estimate of the dimensionality for the set of snapshots is the value of the eigenvalue index i for which $\lambda^{(i)}/\lambda_{\max} = 0{\cdot}01$. In the present case this is 23.

It is useful to consider the fraction q_N of total energy contained, on average, in the expansion for a given number of terms, where

$$q_N = \sum_{k=1}^{N} \lambda^{(k)} \Big/ \sum_{k=1}^{2M} \lambda^{(k)}. \tag{12}$$

The quantity q_N is plotted versus N in Figure 5. The quantity $1 - q_N$ corresponds to the mean square error of the expansion *for snapshots belonging to the ensemble.* The number of terms retained in an eigenfunction expansion depends largely on the degree of accuracy required. However, this decision should be made keeping the behaviour of the above two figures in mind. Specifically, we see that they can be viewed roughly as two piecewise linear segments which connect when the index is about 15–20. We see the same kind of behaviour when we approximate a realization from outside of the ensemble (see Figure 9). From this it is clear that there are two rates of convergence, each corresponding to one leg of the curve. Thus information is captured most rapidly until about 15–20 terms, after which the rate of convergence for both the reconstruction and approximation falls off.

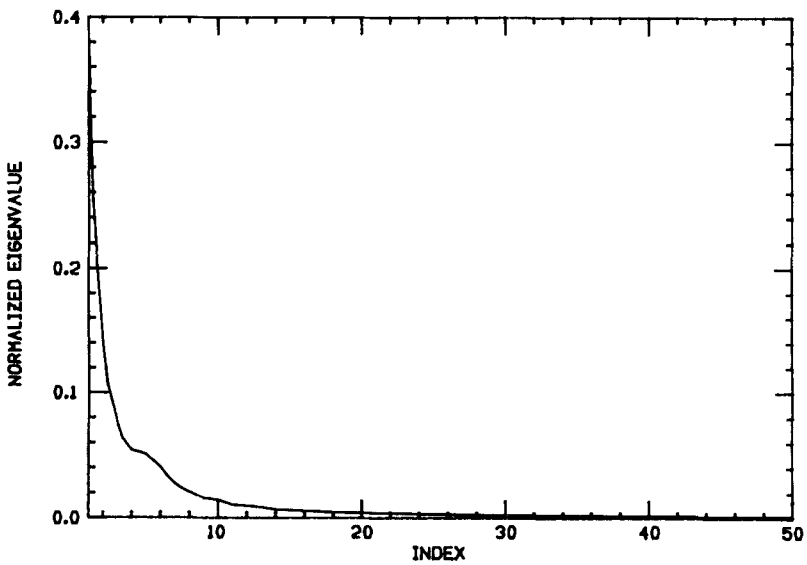

Figure 4. Normalized eigenvalue $\lambda^{(i)}/\Sigma_i \lambda^{(i)}$ versus i

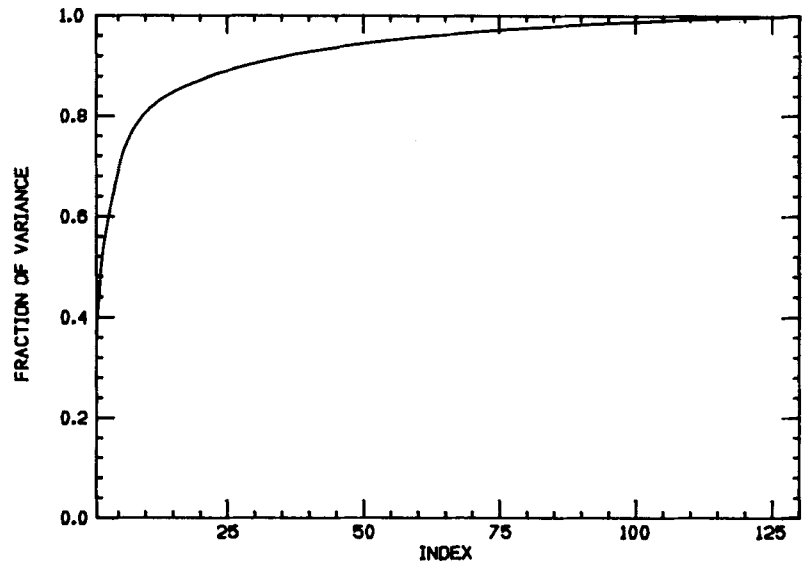

Figure 5. Fraction q_N of total variance as a function of N

5.3. *Eigenflows*

Interpreting the eigenflows is feasible since we have knowledge of several flow variables. As mentioned previously, it should be kept in mind that the eigenflows are not solutions of the flow equation; in fact, they do not in general even satisfy the continuity equation (1a). Hence, while we attribute physical meanings to them, they do not in fact represent physics *per se*.

The first two components, i.e. the u- and v-components of momentum density, of the eigenfunction corresponding to the largest eigenvalue are shown in a momentum density vector plot in Figure 6(a). This eigenfunction, taken with the corresponding pressure component (Figure 6(b)), accounts for 37% of the statistical variance of the flow. It has even symmetry in the sense that $\rho u(x, y) = \rho u(-x, -y)$ and $\rho v(x, y) = \rho v(-x, -y)$. We can observe three large-scale features in the flow. There are a pair of vortices separated by a momentum flux through the centre of the two plates. Note that the direction of the momentum flux is along the shocks. The first pressure eigenfunction is odd, i.e. $p(x, y) = -p(-x, -y)$ has four large-scale structures. Two of the features represent the intensity of the shocks, and it is interesting to note that these intensities are, on average, uneven. The magnitude of the other two structures is about one-seventh of the two in the centre (they are not visible in the blown-up region shown). Here again, the pressure on the edge of the plates is seen to be uneven.

The second eigenfunction, shown in Figure 7, represents 14% of the variance of the flow. The momentum density plot shows two vortex structures separated by momentum flux along the gap. We also see momentum flux along the plate in what are typically low-pressure regions of the flow. The corresponding pressure component of the eigenfunction has three extrema (as well as their corresponding odd counterparts), alternating in sign.

Whereas the momentum density components of the first two eigenfunctions correspond to mass flux through or across the plate, the third eigenfunction represents vorticity in the centre of the slot (Figure 8). There is also a vortex of smaller radius on either side of the centre vortex. This eigenfunction represents 8% of the variance of the flow.

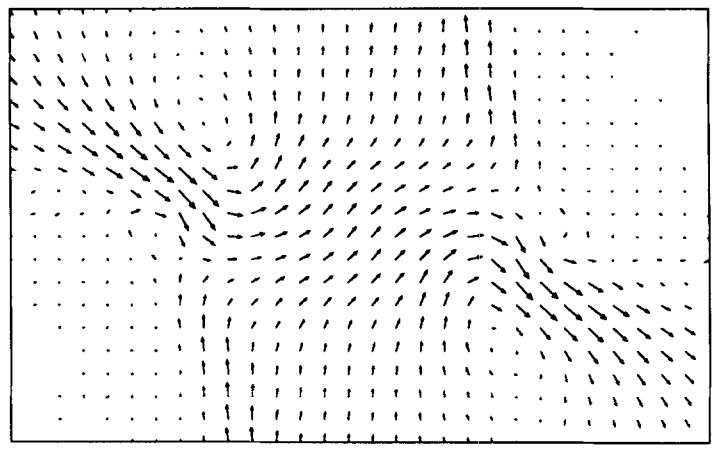

(a)

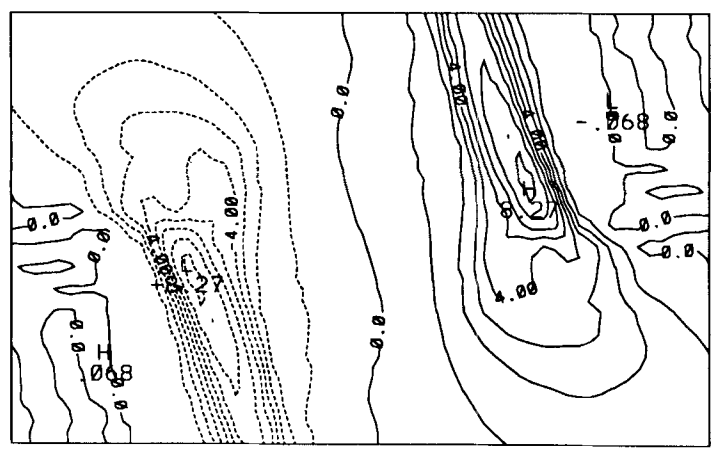

(b)

Figure 6. (a) Momentum density components of first eigenflow, (b) Pressure component of first eigenflow

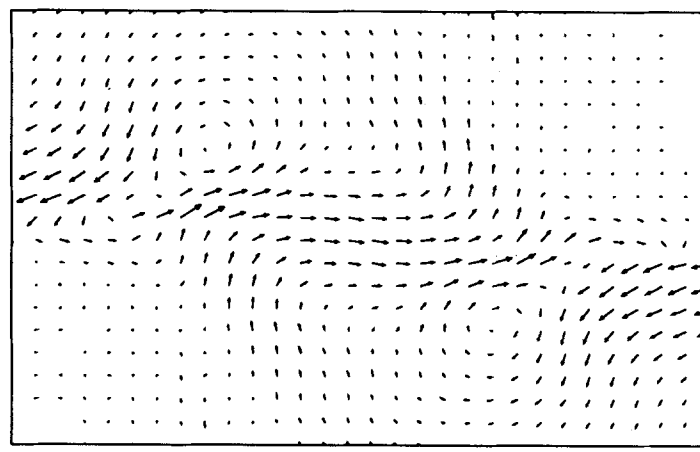

(a)

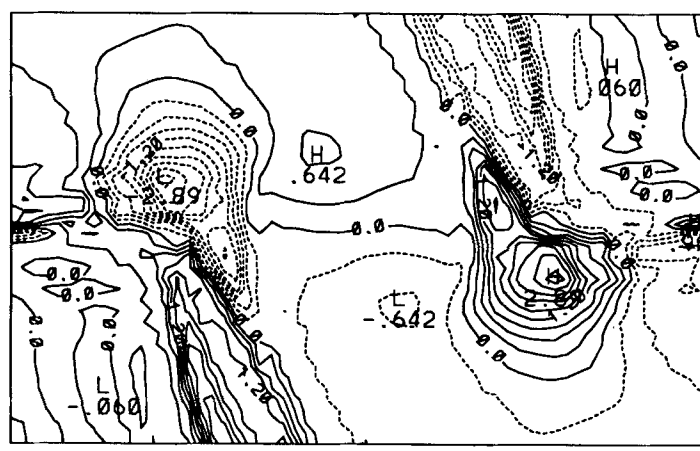

(b)

Figure 7. (a) Momentum density components of second eigenflow. (b) Pressure component of second eigenflow

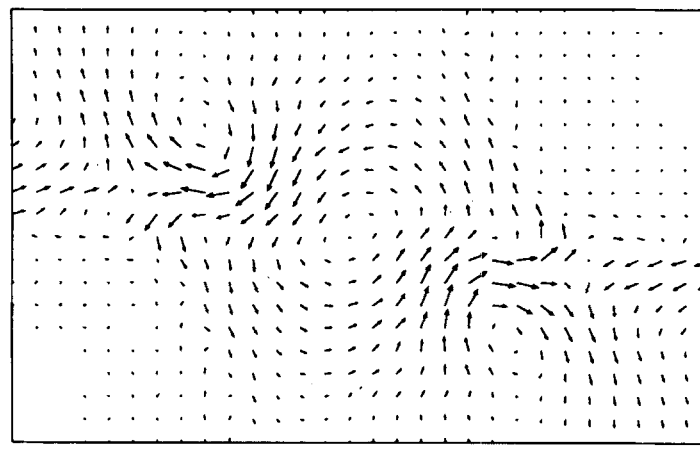

(a)

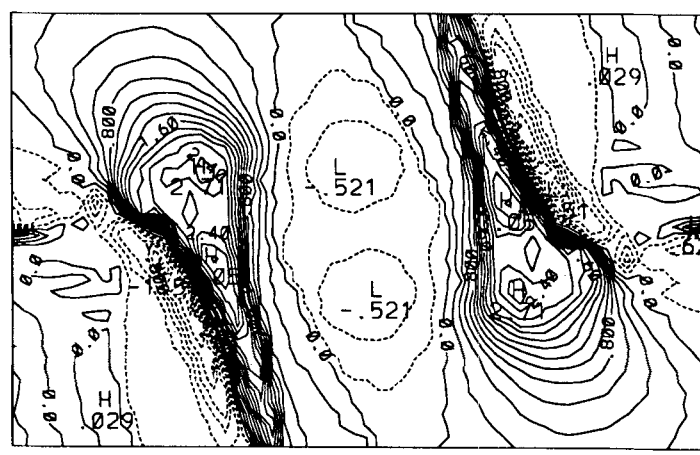

(b)

Figure 8. (a) Momentum density components of third eigenflow. (b) Pressure component of third eigenflow

As the amount of variance associated with each eigenfunction decreases, we see an increasing number of vortices in each momentum density plot and an increased representation of smaller flow scales. The ninth eigenfunction has an interesting shear layer diagonal to the centre of the slot. By this stage each eigenfunction represents less than 2% of the variance of the flow.

The higher-order pressure components of the eigenfunction are generally thin *shock-like structures*. It is apparent that they contribute to the resolution of the shock boundary and steep pressure gradients which occur at different locations in each realization.

5.4. Reconstructions and approximations

As discussed earlier, to test the success of the method we approximate two typical fluctuating flow fields chosen at random, both shown in Figure 3. As observed earlier, the large-scale structure of these fields is very different. We emphasize that the first realization (Figures 3(a) and 3(b)) is a member of the ensemble used in computing the basis set, while the second realization (Figures 3(c) and 3(d)) *is not* (Figure 9).

After only 10 terms the large-scale structure of each realization has been remarkably well captured; see Figures 10–13. The pressure field approximations in Figures 11 and 13 show that the lobes and locations of the shocks are well resolved. However, the steep gradient of the shock has been smoothed somewhat in the approximation. Pictorially the momentum density approximations are uniformly accurate. The error E_{20} is 3·4% for the reconstruction shown in Figure 10(b) and 5·1% for the approximation shown in Figure 12(b). By retaining more terms in the expansion we increasingly resolve the smaller scales of the flow. It is evident that if the ensemble were large enough, i.e. every possible realization is linearly dependent on it, then we would be able to approximate any snapshot with arbitrary precision.

The quantitative errors need more than a visual assessment to put them in perspective. One possible interpretation of the significance of the magnitude of E_N is to consider the average

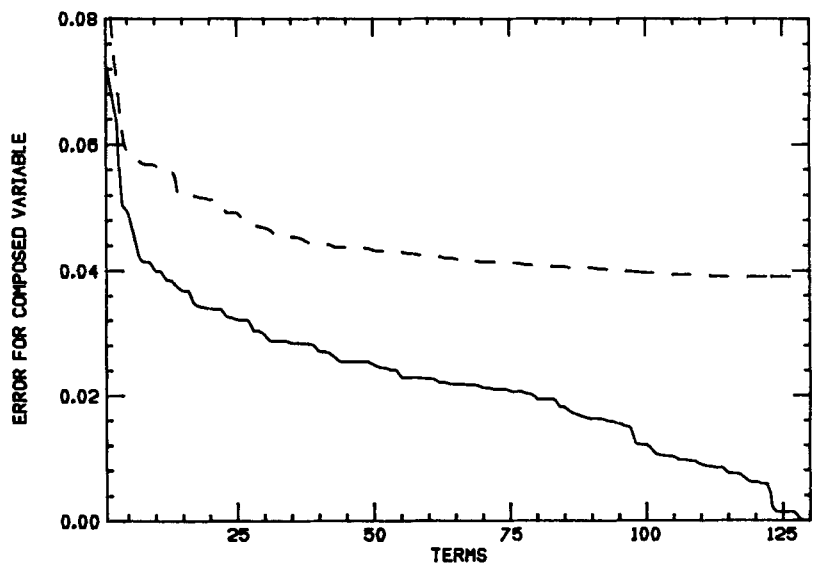

Figure 9. The solid curve corresponds to the reconstruction error E_N for the flow in Figures 3(a) and 3(b). The dashed curve is the approximation error for Figures 3(c) and 3(d) (it is not an ensemble member)

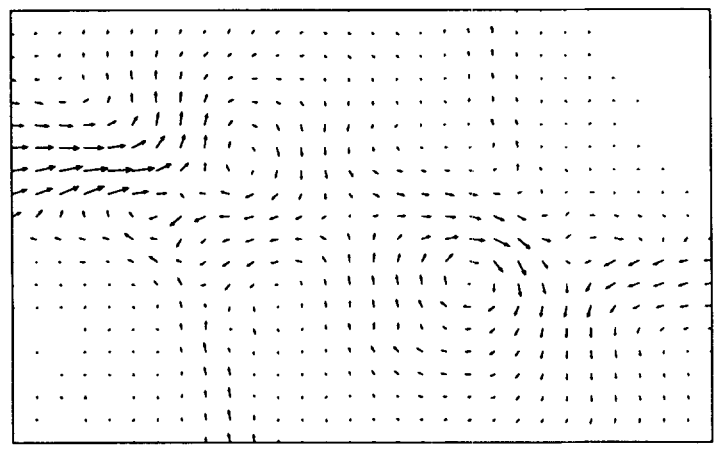

(a)

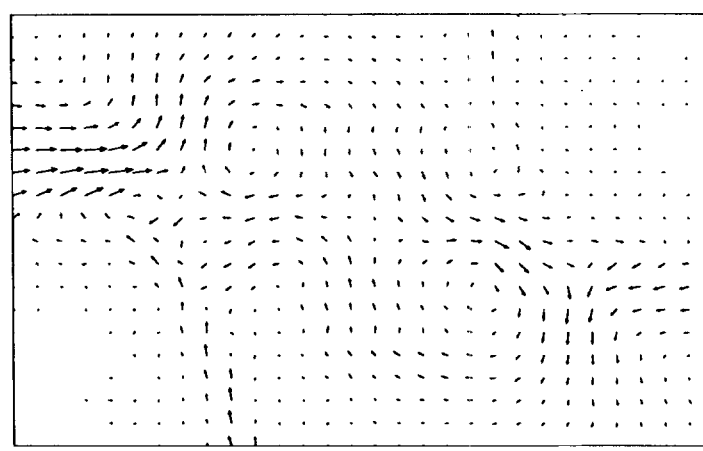

(b)

Figure 10. Momentum density components of the approximation of Figure 3(a) for (a) 10 terms and (b) 20 terms

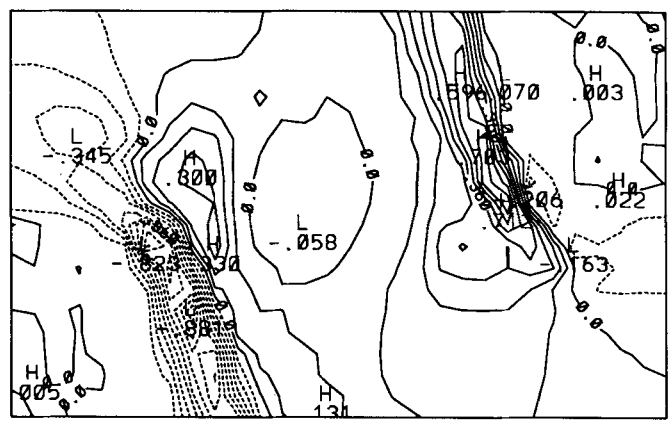

(a)

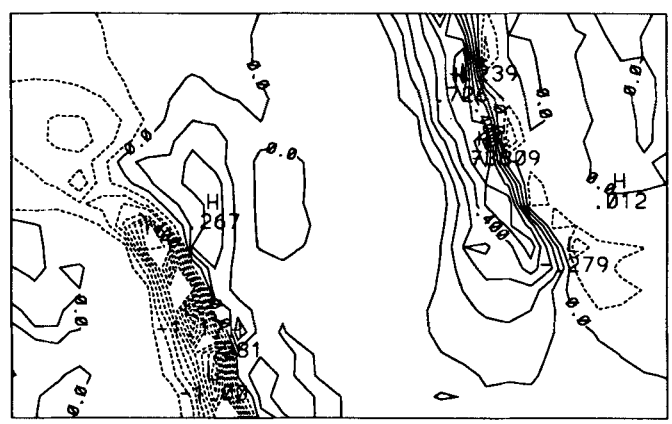

(b)

Figure 11. Pressure field component of the approximation of Figure 3(b) for (a) 10 terms and (b) 20 terms

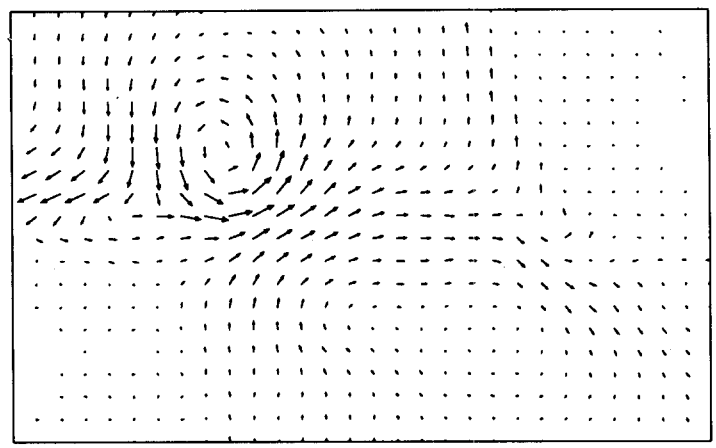

(a)

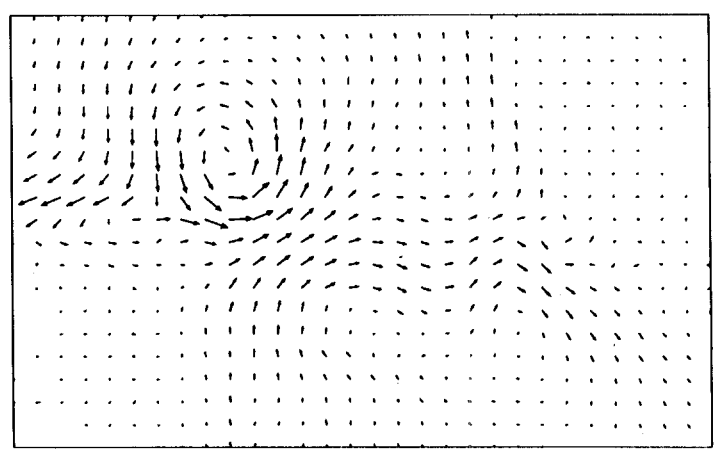

(b)

Figure 12. Momentum density components of the approximation of Figure 3(c) for (a) 10 terms and (b) 20 terms

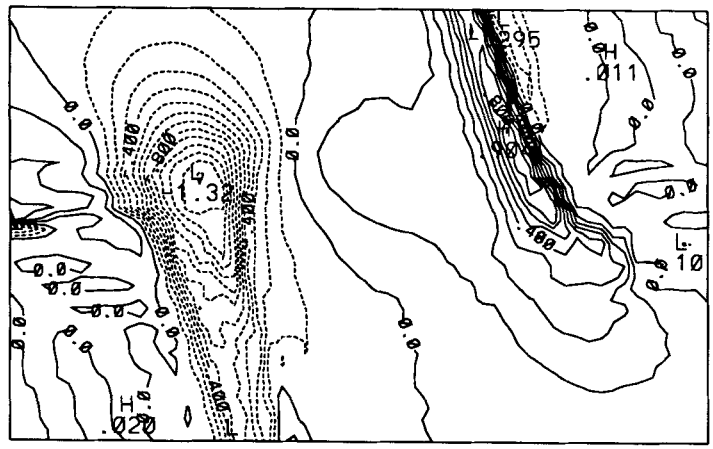

(a)

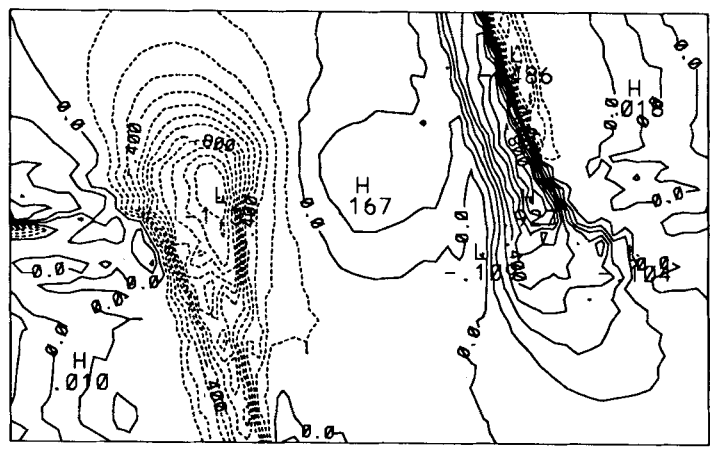

(b)

Figure 13. Pressure field component of the approximation of Figure 3(d) for (a) 10 terms and (b) 20 terms

distance between the flow being approximated and the totality of flows in the ensemble. This error has been computed to be 1·41 (with respect to the fluctuating quantities). Thus, if we view the flows as points in a high-dimensional space and an N-term approximation as a ball of radius r_N, we see that the space is well separated. Specifically, the distance to other points in the space is clustered around 1·41, while the distance to the approximated flow is already less than 0·44 (also with respect to fluctuating quantities) for just 10 terms.

6. DISCUSSION

One underlying theme of the procedure is that of data compression. The 20-term approximation, which captures the large-scale features of a flow, corresponds to a data compression factor of

480:1. A more detailed 100-term approximation captures the smaller scales of the flow and corresponds to a compression ratio of about 100:1. One might hope to do even better with a larger ensemble of flow realizations or a quantitative strobe condition using one or two global quantities to characterize the flow.

A shortcoming of the above approach is that we have essentially eliminated time dependence in a flow with very interesting dynamics. This can be remedied using a simple extension of the above results. An obvious approach would be to strobe the flow at equally spaced intervals in time, and each snapshot would then contribute to a set of ensembles. It would then be possible to compute the eigenfunctions of each covariance matrix, i.e. each ensemble, thus producing a time-dependent representation of the eigenfunctions. However, it might be more advantageous to have each realization contribute to a set of ensembles through an appropriate weighting factor. This modification is presently being investigated.

ACKNOWLEDGEMENTS

We would like to thank Theodore Young for his efforts on GAPS and the Reactive Flow Model wich made these computations possible. The research reported here was supported in part by DARPA/URI contract N00014-86-K0754.

REFERENCES

1. B. J. Cantwell, Organized motion in turbulence', *Ann. Rev. Fluid Mech.*, **13,** 457–515 (1981).
2. J. L. Lumley, 'The structure of inhomogeneous turbulent flows', in A. M. Yaglom and V. I. Tatarski (eds), *Atmospheric Turbulence and Radio Wave Propagation*, Nauka, Moscow, 1967, pp. 166–178.
3. J. L. Lumley, 'Coherent structures in turbulence', in R. E. Meyer (ed.), *Transition and Turbulence*, Academic Press, New York, 1981, pp. 215–242.
4. J. L. Lumley, *Stochastic Tools in Turbulence*, Academic Press, New York, 1970.
5. L. Sirovich, 'Turbulence and the dynamics of coherent structures, Part III: Dynamics and scaling', *Q. Appl. Math.*, **XLV** (3), 583–590 (1987).
6. L. Sirovich, 'Chaotic dynamics of coherent structures', *Physica D*, **37,** 126–145 (1989).
7. L. Sirovich, 'Turbulence and the dynamics of coherent structures, Part I: Coherent structures', *Q. Appl. Math.*, **XLV** (3), 561–571 (1987).
8. K. Fukunaga, *Introduction to Statistical Pattern Recognition*, Academic Press, New York, 1972.
9. H. Hotelling, 'Analysis of a complex of statistical variables into principal components', *J. Educ. Psychol.* (September 1933).
10. M. M. Loève, *Probability Theory*, Van Nostrand, Princeton, NJ, 1955.
11. K. Karhunen, *Ann. Acad. Sci. Fennicae, Ser. A1, Math. Phys.*, **37,** 1–79 (1946).
12. S. Watanabe, 'Karhunen–Loève expansion and factor analysis: theoretical remarks and applications', *Proc. 4th Prague Conf. on Information Theory*, Academic Press (N.Y.) 1965, pp. 635–660.
13. R. B. Ash and M. F. Gardner, *Topics in Stochastic Processes*, Academic Press, New York, 1975.
14. A. K. M. F. Hussain, 'Coherent structures—reality and myth', *Phys. Fluids*, **26,** 2816 (1983).
15. A. K. M. F. Hussain, 'Coherent structures and turbulence', *J. Fluid Mech.*, **173,** 303 (1986).
16. M. Kirby, J. P. Boris and L. Sirovich, 'An eigenfunction analysis of axisymmetric jet flow', *J. Comput. Phys.*, to be published.
17. L. Sirovich, M. Kirby and M. Winter, 'An eigenfunction approach to large scale structures in jet flow', *Phys. Fluids*, **2,** (Feb 1990).
18. J. P. Boris, 'Comments on large eddy simulations using subgrid turbulence models', *Cornell Conference: Wither Turbulence? or Turbulence at the Crossroads*, Cornell University, March 1989.
19. J. P. Boris, E. S. Oran, J. H. Gardner, K. Kailasanath and T. R. Young Jr., 'Computational studies of a localized supersonic shear layer', *AIAA Paper No. 89-0215, 27th Aerospace Sciences Meeting*, Reno, NV, January 1989.
20. E. Oran and J. P. Boris, *Numerical Simulation of Reactive Flow*, Elsevier, New York, 1987.
21. L. Sirovich, 'Turbulence and the dynamics of coherent structures, Part II: Symmetries and transformations', *Q. Appl. Math.* **XLV** (3), 573–582 (1987).
22. M. Kirby and L. Sirovich, 'The application of the Karhunen–Loève procedure for the characterization of human faces', *IEEE Trans. PAMI* **12,** 103–108 (1990).